Implicit Large-Eddy Simulation of a Supersonic Turbulent Boundary Layer: Code Comparison

Jonathan Poggie,* Nicholas J. Bisek,† Timothy Leger,‡ and Ricky Tang§

Air Force Research Laboratory, Wright-Patterson AFB, Ohio 45433-7512 USA

High-fidelity, implicit large-eddy simulations of a Mach 2.9 turbulent boundary layer flow have been carried out using three different computational fluid dynamics codes. The three codes (FDL3DI, HOPS, and US3D) employ the same formal order of spatial and temporal accuracy. The aim of the work was to compare code performance and accuracy, and to identify best practices for large-eddy simulations with the three codes. The simulations were carried out using the same boundary conditions, body force trip mechanism, grids, and time-step. Additional calculations were carried out to compare the results obtained with different numerical algorithms, and to explore correlations characterizing large-scale structures in the flow turbulence. All three codes were able to produce plausible turbulent boundary layers, and showed good agreement in the region where the boundary layer was well developed. The details of the transition process, however, varied with the numerical method and the details of its execution. In particular, coarser grids and more dissipative numerical schemes led to delayed transition to turbulence in the calculations. The body-force trip method was employed successfully in each case, and should be suitable for general application. Many of the features of the large-scale structures were found to match between computation and experiment, but additional work is warranted to explore the use of such comparisons to validate large-eddy simulation codes.

I. Introduction

Large-eddy simulation (LES) is becoming a useful engineering tool for the design of high-speed air vehicles. While Reynolds-averaged Navier-Stokes (RANS) simulations can be effective for flows with weak boundary layer effects, they generally perform poorly for flows with strong three-dimensionality, and very poorly for separated flows. Large-eddy simulation may be able to fill this gap in the portfolio of computational tools for aircraft design. It is thus important to assess the accuracy of large-eddy simulation as an engineering tool, in particular to investigate how the omission of the small scales affects the structure of the flow turbulence, and how the choice of numerical algorithm and code implementation affects the computational results.

In the present project, high-fidelity, implicit large-eddy simulations (HFILES) of a supersonic, turbulent boundary layer flow were performed using three different high-order computational fluid dynamics codes: FDL3DI[1,2] and HOPS,[3–6] developed at the Air Force Research Laboratory, and US3D,[7,8] developed at the University of Minnesota. The FDL3DI code has been extensively validated for large-eddy simulation, and a growing body of work is being produced with US3D. The HOPS code was developed for plasma simulations, but has been recently been adapted for large-eddy simulation.

Both FDL3DI and HOPS are finite-difference, structured-grid codes, whereas US3D is an unstructured, finite-volume code. All three codes can employ sixth-order accurate spatial discretization and second-order accurate, implicit time advancement. The simulations were performed using the same grids, time-step, and numerical trip. With three different, independent code implementations, the comparison of numerical results helps to identify errors in coding and procedure, and assess the relative merits of the numerical algorithms. This project has also proved to be a useful exercise for identifying best practices for carrying out large-eddy simulations with the three codes.

*Senior Aerospace Engineer, Aerospace Systems Directorate. Associate Fellow AIAA.

†Research Aerospace Engineer, Aerospace Systems Directorate. Senior Member AIAA.

‡Research Scientist, Ohio Aerospace Institute. Member AIAA.

§Research Scientist, Universal Technology Corporation. Presently at Sandia National Laboratory. Member AIAA.

II. Numerical Methods

High-fidelity, implicit large-eddy simulations were carried out with three, independently implemented computer codes. The baseline numerical scheme for all three solvers included nominally sixth-order accurate spatial differencing, and implicit, second-order accurate time integration. All three codes include the option of switching to a lower-order, upwind scheme in the vicinity of a shock. For a general review of higher order numerical methods for high-speed flows, see Pirozzoli.[9]

A. US3D

The US3D code is an unstructured, finite volume solver developed by G. Candler's group at the University of Minnesota.[7] The code solves the compressible Navier-Stokes equations using a cell-centered, finite-volume formulation. For the calculations of both the inviscid and viscous fluxes, gradients of flow variables are computed using a weighted least squares method.[10]

In the present work, the inviscid fluxes were evaluated using the low-dissipation, kinetic energy preserving scheme of Subbareddy and Candler.[8] In this formulation, the inviscid fluxes F are computed as the combination of a non-dissipative symmetric component F_s and an upwinded dissipative component F_d multiplied by a shock detecting switch α:

$$F = F_s + \alpha F_d \tag{1}$$

The parameter $\alpha \in [0, 1]$ is chosen so that the dissipative portion of the flux evaluation is only used in regions near discontinuities. The present work employed the Ducros[11] switch:

$$\alpha = \frac{\left(\vec{\nabla} \cdot \vec{u}\right)^2}{\left(\vec{\nabla} \cdot \vec{u}\right)^2 + \|\vec{\omega}\|^2} \tag{2}$$

where $\vec{u}$ and $\vec{\omega}$ are the velocity and vorticity vectors, respectively.

Spatial derivatives of the inviscid fluxes were evaluated using a sixth-order accurate, gradient-based interpolation scheme[12] with the following form:

$$\phi_{i+\frac{1}{2}} = \frac{\phi_i + \phi_{i+1}}{2} + \frac{8(\delta\phi_i + \delta\phi_{i+1})}{15} - \frac{\delta\phi_{i-1} + \delta\phi_{i+2}}{45} \tag{3}$$

Here $\delta\phi_i$ is the scalar (dot) product of the gradient of ϕ in Cell i and the vector from the center of Cell i to the center of Face $i + \frac{1}{2}$. The viscous fluxes were evaluated using a second-order accurate central difference scheme.

The current computations were carried out using the perfect gas assumption. Second-order accurate, implicit time integration was employed.[13]

B. HOPS and FDL3DI

Two codes developed at the Air Force Research Laboratory (AFRL) were also used in this study. The FDL3DI code[1,2] was named for the Flight Dynamics Laboratory, a precursor organization to AFRL. This code is a high-order accurate, structured-grid, finite-difference solver for the perfect-gas, compressible-flow Navier-Stokes equations. The HOPS (Higher Order Plasma Solver) code[3–6] is a multi-fluid code developed for plasma computations. The code includes several physical models, but here it is employed as a single-fluid gasdynamics code. Employed in this way, the two codes represent independent implementations of essentially the same numerical approach.

Time integration of the conservation equations was carried out in the baseline approach using a second-order implicit scheme, based on a three-point backward difference of the time terms. The general formulation is similar to the standard technique of Beam and Warming.[14] Approximate factoring and quasi-Newton subiterations were employed, with three applications of the flow solver per time step. The implicit terms were evaluated using the scalar pentadiagonal formulation of Pulliam and Chaussee.[15] For comparison, a fourth-order, explicit Runge-Kutta method was employed for some of the calculations.

The baseline spatial differencing scheme was based on compact differencing and filtering.[1,16] In one dimension, the finite difference approximation to the first derivative ϕ'_i at Node i is evaluated by solving a

Parameter	Value
δ_0	5.375 mm
U_∞	604.5 m/s
p_∞	2.303 kPa
T_∞	108.1 K
T_w	269.5 K
M_∞	2.9
U_∞/ν_∞	6.0×10^6 m^{-1}

Table 1. Flow conditions for Mach 2.9 turbulent boundary layer.

tridiagonal system of the form:

$$\alpha\phi'_{i-1} + \phi'_i + \alpha\phi'_{i+1} = a\,\frac{\phi_{i+1} - \phi_{i-1}}{2} + b\,\frac{\phi_{i+2} - \phi_{i-2}}{4} \tag{4}$$

where α, a, and b are constants chosen to give a certain order of accuracy and set of spectral properties for the scheme.

Numerical stability was enforced using a low-pass, Padé-type, non-dispersive spatial filter. The filtering approach replaces the computed value ϕ_i at a particular node with a filtered value $\overline{\phi}_i$:

$$\alpha_f\overline{\phi}_{i-1} + \overline{\phi}_i + \alpha_f\overline{\phi}_{i+1} = \sum_{n=0}^{N} \frac{a_n}{2}(\phi_{i+n} + \phi_{i-n}) \tag{5}$$

where the constants α_f, a_0, ... a_N are chosen to give appropriate filter properties. The filter was applied to the solution vector, sequentially, in each of the three computational directions, following each sub-iteration for implicit time integration, or each time-step for explicit integration. The order of the filtering operation was permuted at each time step.

The hybrid compact-Roe shock capturing scheme of Visbal and Gaitonde[2] is employed for flows containing strong shocks, but this was not necessary in the present work. For comparison to the compact difference computations, an additional set of conventional upwind calculations was carried out with a third-order, upwind-biased Roe scheme,[17–20] and fourth-order explicit spatial differencing of the viscous and metric terms. These computations did not employ a limiter or filter.

The metrics were evaluated using the method of Thomas and Lombard.[21]

III. Results

The baseline flow investigated here consists of a Mach 2.9, flat-plate turbulent boundary layer. The flow conditions are listed in Table 1, and correspond to those reported for the experiments of Bookey et al.,[22] and studied in a number of previous computations.[23] The conditions in the experiments of Spina[24] are similar, but correspond to an order of magnitude higher Reynolds number.

The calculation procedure was the same for each of the three computer codes. The inflow boundary condition was provided by a similarity solution of the compressible, laminar boundary layer equations. The boundary layer was tripped to turbulence using the body-force trip method of Mullenix et al.[25] No-slip conditions were imposed on the flat-plate surface, with zero normal pressure gradient enforced to third-order accuracy. Periodic boundary conditions were imposed in the spanwise direction. Grid stretching and extrapolation were used to provide outflow boundary conditions.

Two different computational meshes were employed: a coarse grid of 1.1×10^7 points and a fine grid of 7.7×10^7 points. The streamwise extent of the resolved region was $100\delta_0$ and the spanwise extent was $5\delta_0$. Some details of the two grids are listed in Table 2, and the fine mesh is illustrated in Fig. 1.

Table 2 also provides the grid spacing nondimensionalized in inner coordinates using reference conditions at the station $x/\delta_0 = 100$. For flat plate configurations, Georgiadis et al.[26] recommend $50 \le \Delta x^+ \le 150$, $\Delta y^+_{\text{wall}} < 1$, and $15 \le \Delta z^+ \le 40$ for well-resolved large-eddy simulations, and $10 \le \Delta x^+ \le 20$, $\Delta y^+_{\text{wall}} < 1$,

Quantity	Coarse Mesh	Fine Mesh
N_x	677	1161
N_y	131	261
N_z	130	255
$\Delta x/\delta_0$	2.0×10^{-1}	1.0×10^{-1}
$\Delta y_{\text{wall}}/\delta_0$	4.0×10^{-3}	2.0×10^{-3}
$\Delta z/\delta_0$	4.0×10^{-2}	2.0×10^{-2}
Δx^+	50	28
Δy^+_{wall}	1.0	0.55
Δz^+	10	5.5
$U_\infty \Delta t/\delta_0$	1.0×10^{-3}	1.0×10^{-3}
Δt^+	1.1×10^{-2}	1.2×10^{-2}
Re_θ	5.3×10^3	5.7×10^3

Table 2. Properties of the computational mesh, nondimensionalized using conditions in the vicinity of the reference station $x/\delta_0 = 100$ (HOPS code, C6/F8 scheme).

and $5 \leq \Delta z^+ \leq 10$ for direct numerical simulations. They recommend time steps in the range $\Delta t^+ < 1$. Both grids meet the criteria for well-resolved large-eddy simulation, but not the criteria for direct numerical simulation. In particular, the spacing is relatively coarse in the streamwise direction (x), about a factor of 2.5 too large to meet the recommendations for DNS.

Laminar flow calculations were carried out as a basic check of the codes (Fig. 2). These calculations were carried out on the coarse mesh, in the absence of a boundary layer trip. The similarity solution was provided as the inflow profile at $x = 0$, and a laminar boundary layer developed along the plate in the computations. Boundary layer profiles are shown in Fig. 2a for the $x/\delta_0 = 100$ station, corresponding to the end of the well-resolved region of the computational mesh. The computational results are seen to be in close agreement with the boundary layer similarity solution (marked "Theory"). The normalized skin friction coefficient $C_f \text{Re}_x^{1/2}$ is shown as a function of streamwise distance x/δ_0 along the plate center in Fig. 2b. Again, the agreement between the calculations and the similarity solution is very close.

A. Basic Results

Figure 3 shows an example of an instantaneous flow solution obtained with the HOPS code on the fine grid for the turbulent boundary layer flow. The location of the boundary layer trip is apparent at $x/\delta_0 = 2.5$, both as a bump in the temperature isosurface, and as a Mach wave in the density contours. The flow is transitional in the region up to about $x/\delta_0 = 30$, but farther downstream it appears to be fully turbulent.

To illustrate the region of the flow considered in the detailed analysis presented next, cross-sections of the instantaneous flowfield are given in Fig. 4 and Fig. 5. All the plots correspond to the same instant in time.

Figure 4 shows instantaneous contours of the streamwise mass flux ρu, a quantity that can be measured experimentally with hotwire probes.[27] Three planes are shown: an end view in the $x/\delta_0 = 100.00$ plane, a plan view in a plane about halfway through the boundary layer ($y/\delta_0 = 1.43$ or $y/\delta = 0.55$), and a side view plane at the center of the domain ($z/\delta_0 = 2.50$). In all the plots, the highly convoluted interface between the boundary layer and the freestream is apparent. Boundary layer fluid appears to be ejected beyond the mean boundary layer edge ($\delta/\delta_0 \approx 2.6$), and freestream fluid often reaches close to the wall. Within the sectional planes, islands of freestream fluid are sometimes visible wholly surrounded by boundary layer fluid, as are disconnected islands of boundary layer fluid in the freestream. These results are qualitatively consistent with those of flow visualization experiments.[28]

Corresponding plots of quantities at the wall ($y = 0$) are shown in Fig. 5. Wall pressure fluctuations in turbulent boundary layer flows have been the subject of extensive experimental investigation.[29] Figure 5a shows the instantaneous wall pressure, and Fig. 5b shows the magnitude of the wall shear stress. (Shear stress was computed in a post-processing step, using the same compact difference formulation as for the flow

solution.) Structures in the pressure field appear relatively isotropic, whereas structures in the shear stress are elongated in the streamwise direction.

Basic statistical properties of the turbulent boundary flow are given in Fig. 6 for computations employing the HOPS code on each of the two grids. These calculations were carried out using a sixth-order compact difference scheme with eighth-order filtering (C6/F8). Figure 6a shows the skin friction coefficient, averaged in time and across the spanwise direction. Transition is seen to be delayed on the coarse grid relative to the fine grid, with a lower skin friction coefficient in the fully turbulent flow. Profiles of the mean streamwise velocity are shown in van Driest transformed coordinates[30] in Fig. 6c for the $x/\delta_0 = 100$ station. The velocity profile for the fine grid case matches theory closely, but the coarse grid case is still transitional.

The effect of the filtering on the transition process is also of interest. The effect of using different filter coefficients in Eq. (5) is shown in Fig. 7. (The filtering method is explained in detail in Refs. 1,16.) Filtering can be carried out for values of the filter coefficient of $-0.5 < \alpha_f < 0.5$, with values closest to $\alpha_f = 0.5$ giving the sharpest cut-off. Here we see that more severe filtering delays transition somewhat, but the effect is not very strong for the typical range of filtering coefficients employed with this numerical approach.

Statistical properties of the turbulent boundary flow are given in Fig. 8 for computations carried out using three different spatial discretization schemes implemented in the HOPS code: a sixth-order compact difference scheme (labelled C6), a fourth-order scheme based on an explicit stencil (E4), and a nominally third-order, upwind-biased implementation of the Roe scheme (ROE3). An eighth-order filter (F8) was used for the sixth-order compact difference scheme, but cases with both sixth-order (F6) and eighth-order filters were examined with the explicit fourth-order spatial scheme. An additional case was run with the sixth-order compact difference scheme using fourth-order Runge-Kutta time integration (RK4) rather than the baseline implicit time integration scheme. For these explicit calculations, the nondimensional time step was reduced to $\Delta t = 5 \times 10^{-4}$. The results of all the computations are in qualitative agreement, but the more dissipative spatial discretization approaches are seen to predict a delayed transition to turbulence.

A comparison of the results obtained with the different computational fluid dynamics codes is presented in Fig. 9 for the fine grid. The sub-figures show the mean profiles of skin friction, momentum thickness, streamwise velocity, and a form of the Reynold stress. The transition process is seen to vary slightly for the different codes and numerical approaches. Nonetheless, a well-developed turbulent boundary layer profile is obtained for each case, and the profiles agree closely when cast in nondimensional coordinates.

For reference, Fig. 10 compares the velocity profiles obtained in the present study using the HOPS code on the fine grid ($x/\delta_0 = 100$, $\mathrm{Re}_\theta = 5.7 \times 10^3$) with those published by Spina[24] ($\mathrm{Re}_\theta = 8.1 \times 10^4$). The profiles are presented both in outer variables (Fig. 10a) and van Driest transformed inner variables (Fig. 10b). The results are as expected for two well-developed turbulent boundary layers with an order-of-magnitude difference in Reynolds number. The near-wall region differs in outer variables and the wake region differs in inner variables. Reasonable agreement is obtained in the logarithmic region.

B. Correlations

It is of interest to evaluate the ability of large-eddy simulation to predict the properties of δ-scale structures, which are resolved in this approach. Here we focus on cross-correlations of various flow quantities, using the results of simulations with the HOPS code that employed the sixth-order compact difference scheme, eighth-order filtering, and implicit time advancement. For all the correlation statistics, averaging was performed for at least one domain flow-through time (1×10^5 iterations).

Time series of the fluctuations of mass flux generated by the simulations were saved in order to carry out the correlation analysis. The analysis is intended to be similar to that employed in the classic hotwire studies of Kovasznay et al.[31] in a low-speed turbulent boundary layer, and of Spina et al.[24,32,33] in a supersonic boundary layer.

Space-time correlations are shown in Fig. 11. Both cases shown correspond to a streamwise station of $x/\delta_0 = 97.0$, with a corresponding momentum thickness Reynolds number of $\mathrm{Re}_\theta = 5.5 \times 10^3$. If Taylor's hypothesis[34] is applied to convert time to an effective streamwise coordinate, Fig. 11a can be interpreted as a side-view image of the flow in the center plane ($z/\delta_0 = 2.50$). The reference point for the correlations is set at $y_{\mathrm{ref}}/\delta = 0.55$, and the surrounding correlation contours indicate the characteristic inclination of the large-scale boundary layer structures. (Here, the boundary layer thickness is $\delta/\delta_0 \approx 2.6$.)

Figure 11b shows the corresponding plan-view correlation, for the $y/\delta = 0.55$ plane, with $z_{\mathrm{ref}}/\delta_0 = 2.5$. Again using Taylor's hypothesis to interpret time as a surrogate spatial coordinate, we note a characteristic elongation of the correlation contours in the streamwise direction.

Figure 12 compares space-time correlations in a horizontal plane between the computations and the experiments of Spina.[24] The experimental data correspond to nearly the same nondimensional distance from the wall ($y/\delta = 0.51$), but a higher Reynolds number. The shape of the correlation contours differs somewhat between computation and experiment, perhaps due to issues of spatial resolution. Nonetheless, the characteristic scale of the $R = 0.3$ correlation contour is about 0.5δ in both cases.

Spatial correlations are shown in Fig. 13. (See Fig. 4 for plots of the instantaneous mass-flux in the same planes.) The similarities between Fig. 11a and Fig. 13a, and between Fig. 11b and Fig. 13b, suggest that Taylor's hypothesis is a good approximation for this flow.

The scale and orientation of the large-scale structures in the simulated boundary layer are similar to those observed in experiments.[31] The mass flux is well-correlated over a length scale on the order of the mean boundary layer thickness δ, and the correlation contours are roughly ellipsoidal. The characteristic length in the spanwise direction is somewhat smaller than that in the wall-normal or streamwise directions, and contours in the x-y-plane are oriented at an angle of about 45 deg from the wall. These results are generally consistent with the appearance of the instantaneous mass-flux field seen in Fig. 4.

Broad-band convection velocities, derived from space-time cross-correlations of the mass flux fluctuations, are shown in Fig. 14. The convection velocity is determined by dividing the distance between two stations separated in the streamwise direction by the time delay for optimal correlation of the signals obtained at the two stations. Computational results referenced to the $x/\delta_0 = 98$ station are shown in Fig. 14a. The convection velocity profile is seen to closely match the mean velocity profile, which is included for comparison.

The corresponding results obtained by Spina et al.[33] from hotwire measurement are shown in Fig. 14b. Those results show $U_c/U_\infty = 0.9 \pm 0.1$ across the outer part of the boundary layer. (The experimental uncertainty was primarily due to temporal discretization, the sampling rate of the analog-to-digital converter.) Because of the large error bar on the experimental data, it is difficult to say whether the convection velocity is actually constant across the boundary layer, or agrees closely with the mean velocity as seen in the computations. It should also be noted that the streamwise separation of the hotwire probes ($x/\delta = 0.1$ to 0.2) is smaller than that employed in the computational analysis ($x/\delta = 0.5$ to 2.0). We plan to explore these differences carefully in future work.

Another flow variable that has been extensively studied experimentally is the fluctuating wall pressure.[29] Time series of the computed wall pressure fluctuations were saved for correlation analysis. Spatial correlations of the fluctuating wall pressure are shown in Fig. 15. Computational results obtained with the HOPS code are shown in Fig. 15a, and the experimental results of Spina[24] are shown in Fig. 15b. (The experimental data were obtained with four Kulite pressure transducers, mounted in a line at the wall with a spacing of 0.18δ.) For the computations, the correlation contours are roughly circular, with a characteristic diameter of about 0.1δ. These results are qualitatively consistent with the features of the instantaneous wall pressure field shown in Fig. 5a. In contrast, the experimental correlation contours are elongated in the spanwise direction, and the characteristic length scale in the streamwise direction is about twice that obtained computationally. This discrepancy is also a topic of ongoing investigation, focusing in particular on issues of spatial resolution in the measurements.

Convection velocities were also computed for the wall pressure data, again by taking data from two stations separated in the streamwise direction, and dividing the distance between the stations by the time delay for optimal correlation. The results are shown in Fig. 16 as a function of the streamwise separation, and compared to several experimental data sets.[24,35–37] For all data sets, the convection velocity lies in the range $0.60 \leq U_c/U_\infty = 0.90$. The computational results fall in the middle of the range spanned by the experimental measurements.

IV. Summary and Conclusions

We seek to demonstrate that large-eddy simulation can take a productive place in the portfolio of tools for high-speed aircraft design, in particular replacing Reynolds-averaged Navier-Stokes methods for the simulation of highly three-dimensional flows. As a first step in this process, we have undertaken a verification and validation project for large-eddy simulation of compressible, turbulent flow. This paper has presented an initial progress report.

High-fidelity, implicit large-eddy simulations of a Mach 2.9 turbulent boundary layer flow were carried out using three different computational fluid dynamics codes (FDL3DI, HOPS, and US3D) with the same formal order of spatial and temporal accuracy. The codes FDL3DI and HOPS are finite-difference, structured-grid

solvers, developed at the Air Force Research Laboratory, whereas US3D is an unstructured, finite-volume code, developed at the University of Minnesota. The aim of the work was to compare their performance and numerical accuracy. The simulations were carried out using the same boundary conditions, body force trip mechanism, grids, and time-step. Additional calculations were carried out to compare the results obtained with different numerical algorithms.

All three codes were able to produce plausible turbulent boundary layers, and showed good agreement in the region where the boundary layer was well developed. General agreement was also obtained with experimental turbulent boundary layer profiles. The details of the transition process, however, varied with the numerical method and the details of its execution. In particular, coarser grids and more dissipative numerical schemes led to delayed transition to turbulence in the calculations. The body-force trip method was employed successfully in each case, and should be suitable for general application with different codes and numerical approaches.

Calculations were also carried out to explore correlations characterizing large-scale structures in the flow turbulence. Many of the features of the large-scale structures were found to match between computation and experiment, but additional work is warranted to explore the use of such comparisons to validate large-eddy simulation codes.

Acknowledgments

This project is sponsored in part by the Air Force Office of Scientific Research, under tasks monitored by F. Fahroo and J. Schmisseur, and by grants of High Performance Computing time from the Air Force Research Laboratory (AFRL), Army Research Laboratory (ARL), and Army Engineer Research and Development Center (ERDC) Defense Supercomputing Resource Centers (DSRC).

The authors would like to acknowledge helpful discussions with D. Gaitonde, D. Garmann, R. Gosse, M. Visbal, and M. White.

References

[1]Visbal, M. R. and Gaitonde, D. V., "On the Use of Higher-Order Finite-Difference Schemes on Curvilinear and Deforming Meshes," *Journal of Computational Physics*, Vol. 181, 2002, pp. 155–185.

[2]Visbal, M. R. and Gaitonde, D. V., "Shock Capturing Using Compact-Differencing-Based Methods," AIAA Paper 2005-1265.

[3]Poggie, J., "High-Order Compact Difference Methods for Glow Discharge Modeling," AIAA Paper 2009-1047.

[4]Poggie, J., "Compact Difference Methods for Discharge Modeling in Aerodynamics," AIAA Paper 2009-3908.

[5]Poggie, J., "Role of Charged Particle Inertia in Pulsed Electrical Discharges," AIAA Paper 2010-1195.

[6]Poggie, J., "High-Order Numerical Methods for Electrical Discharge Modeling," AIAA Paper 2010-4632.

[7]Nompelis, I., Drayna, T. W., and Candler, G. V., "A Parallel Unstructured Implicit Solver for Hypersonic Reacting Flow Simulation," AIAA Paper 2005-4867.

[8]Subbareddy, P. K. and Candler, G. V., "A Fully Discrete, Kinetic Energy Consistent Finite-Volume Scheme for Compressible Flows," *Journal of Computational Physics*, Vol. 228, 2009, pp. 1347–1364.

[9]Pirozzoli, S., "Numerical Methods for High-Speed Flows," *Annual Review of Fluid Mechanics*, Vol. 43, 2011, pp. 163–194.

[10]Mavriplis, D. J., "Revisiting the Least-Squares Procedure for Gradient Reconstruction on Unstructured Meshes," NASA/CR 2003-212683, National Aeronautics and Space Administration, Hampton, VA, December 2003.

[11]Ducros, F., Ferrand, V., Nicoud, F., Weber, C., Darracq, D., Gacherieu, C., and Poinsot, T., "Large-Eddy Simulation of the Shock/Turbulence Interaction," *Journal of Computational Physics*, Vol. 152, No. 1, 1999, pp. 199–238.

[12]Bartkowicz, M. D., Subbareddy, P. K., and Candler, G. V., "Numerical Simulations of Roughness Induced Instability in the Purdue Mach 6 Wind Tunnel," AIAA Paper 2010-4723.

[13]Wright, M. J., Candler, G. V., and Prampolini, M., "Data-Parallel Lower-Upper Relaxation Method for the Navier-Stokes Equations," *AIAA Journal*, Vol. 34, No. 7, 1996, pp. 1371–1377.

[14]Beam, R. and Warming, R., "An Implicit Factored Scheme for the Compressible Navier-Stokes Equations," *AIAA Journal*, Vol. 16, No. 4, 1978, pp. 393–402.

[15]Pulliam, T. H. and Chaussee, D. S., "A Diagonal Form of an Implicit Approximate-Factorization Algorithm," *Journal of Computational Physics*, Vol. 39, 1981, pp. 347–363.

[16]Gaitonde, D. V. and Visbal, M. R., "High-Order Schemes for Navier-Stokes Equations: Algorithm Implementation into FDL3DI," Technical Report AFRL-VA-WP-TR-1998-3060, Air Force Research Laboratory, Wright-Patterson Air Force Base, Ohio, August 1998.

[17]Roe, P. L., "Approximate Riemann Solvers, Parameter Vectors, and Difference Schemes," *Journal of Computational Physics*, Vol. 43, 1981, pp. 357–372.

[18]Anderson, W. K., Thomas, J. L., and van Leer, B., "Comparison of Finite Volume Flux Vector Splittings for the Euler Equations," *AIAA Journal*, Vol. 24, No. 9, 1986, pp. 1453–1460.

[19]Morrison, J., "Flux Difference Split Scheme for Turbulent Transport Equations," AIAA Paper 90-5251, 1990.

[20]Gaitonde, D. and Shang, J. S., "Accuracy of Flux-Split Algorithms in High-Speed Viscous Flows," *AIAA Journal*, Vol. 31, No. 7, 1993, pp. 1215–1221.

[21]Thomas, P. D. and Lombard, C. K., "Geometric Conservation Law and Its Application to Flow Computations on Moving Grids," *AIAA Journal*, Vol. 17, No. 10, 1979, pp. 1030–1037.

[22]Bookey, P., Wyckham, C., Smits, A., and Martin, M. P., "New Experimental Data of STBLI at DNS/LES Accessible Reynolds Numbers," AIAA Paper 2005-309.

[23]Wu, M. and Martin, M. P., "Direct Numerical Simulation of Supersonic Turbulent Boundary Layer over a Compression Ramp," *AIAA Journal*, Vol. 45, No. 4, 2007, pp. 879–889.

[24]Spina, E. F., *Organized Structures in a Supersonic Turbulent Boundary Layer*, Ph.D. Dissertation, Princeton University, Princeton NJ, October 1988.

[25]Mullenix, N. J., Gaitonde, D. V., and Visbal, M. R., "Spatially Developing Supersonic Turbulent Boundary Layer with a Body-Force Based Method," *AIAA Journal*, Vol. 51, No. 8, 2013, pp. 1805–1819.

[26]Georgiadis, N. J., Rizzetta, D. P., and Fureby, C., "Large-Eddy Simulation: Current Capabilities, Recommended Practices, and Future Research," *AIAA Journal*, Vol. 48, No. 8, 2010, pp. 1772–1784.

[27]Smits, A. J., Hayakawa, K., and Muck, K. C., "Constant Temperature Hotwire Anemometry Practice in Supersonic Flows, Part I: The Normal Wire," *Experiments in Fluids*, Vol. 1, No. 2, 1983, pp. 83–92.

[28]Poggie, J., Erbland, P. J., Smits, A. J., and Miles, R. B., "Quantitative Visualization of Compressible Turbulent Shear Flows using Condensate-Enhanced Rayleigh Scattering," *Experiments in Fluids*, Vol. 37, 2004, pp. 438–454.

[29]Beresh, S. J., Henfling, J. F., Spillers, R. W., and Pruett, B. O. M., "Fluctuating Wall Pressures Measured Beneath a Supersonic Turbulent Boundary Layer," *Physics of Fluids*, Vol. 23, 2011, pp. 075110.

[30]van Driest, E. R., "On the Turbulent Flow Near a Wall," *Journal of the Aeronautical Sciences*, Vol. 23, 1956, pp. 1007–1011.

[31]Kovasznay, L. S. G., Kibens, V., and Blackwelder, R. F., "Large-Scale Motion in the Intermittent Region of a Turbulent Boundary Layer," *Journal of Fluid Mechanics*, Vol. 41, 1970, pp. 283–325.

[32]Spina, E. F. and Smits, A. J., "Organized Structures in a Compressible, Turbulent Boundary Layer," *Journal of Fluid Mechanics*, Vol. 182, 1987, pp. 85–109.

[33]Spina, E. F., Donovan, J. F., and Smits, A. J., "On the Structure of High-Reynolds-Number Supersonic Turbulent Boundary Layers," *Journal of Fluid Mechanics*, Vol. 222, 1991, pp. 293–327.

[34]Taylor, G. I., "The Spectrum of Turbulence," *Procedings of the Royal Society of London A*, Vol. 164, 1938, pp. 476–490.

[35]Bull, M. K., "Wall-Pressure Fluctuations Associated with Subsonic Turbulent Boundary Layer Flow," *Journal of Fluid Mechanics*, Vol. 28, 1967, pp. 719–754.

[36]Chyu, W. J. and Hanly, R. D., "Power and Cross-Spectra and Space-Time Correlations of Surface Fluctuating Pressures at Mach Numbers Between 1.6 and 2.5," AIAA Paper 68-77.

[37]Tan, D. K. M., Tran, T. T., and Bogdonoff, S. M., "Surface Pressure Fluctuations in a Three-Dimensional Shock Wave / Turbulent Boundary Layer Interaction," AIAA Paper 85-0125.

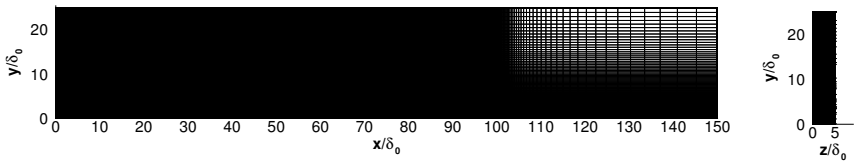

Figure 1. Computational mesh for Mach 2.9 turbulent boundary layer computations (fine grid case).

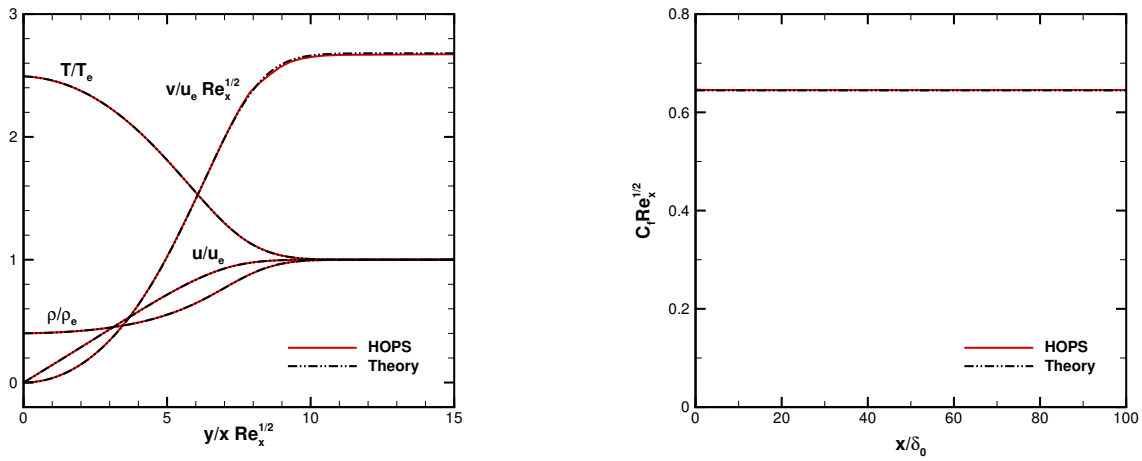

(a) Boundary layer profiles at $x/\delta_0 = 100$.

(b) Skin friction profile.

Figure 2. Mach 2.9 laminar boundary layer flow (HOPS code, coarse grid, C6/F8 scheme).

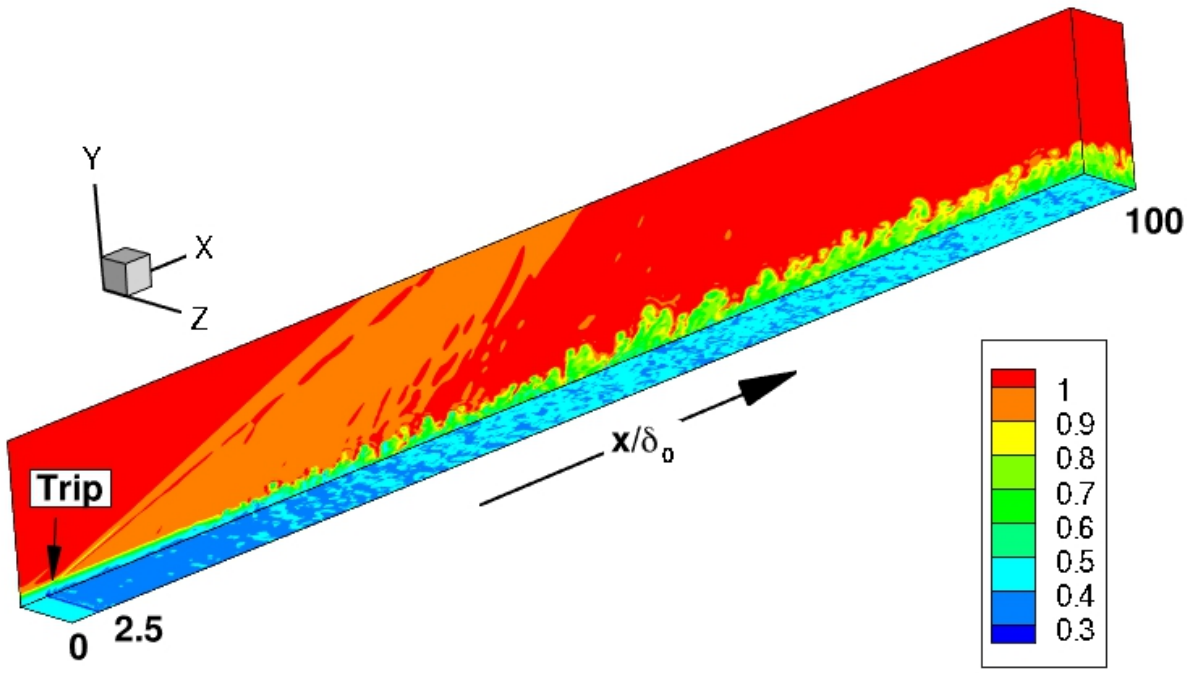

(a) Density contours, ρ/ρ_∞.

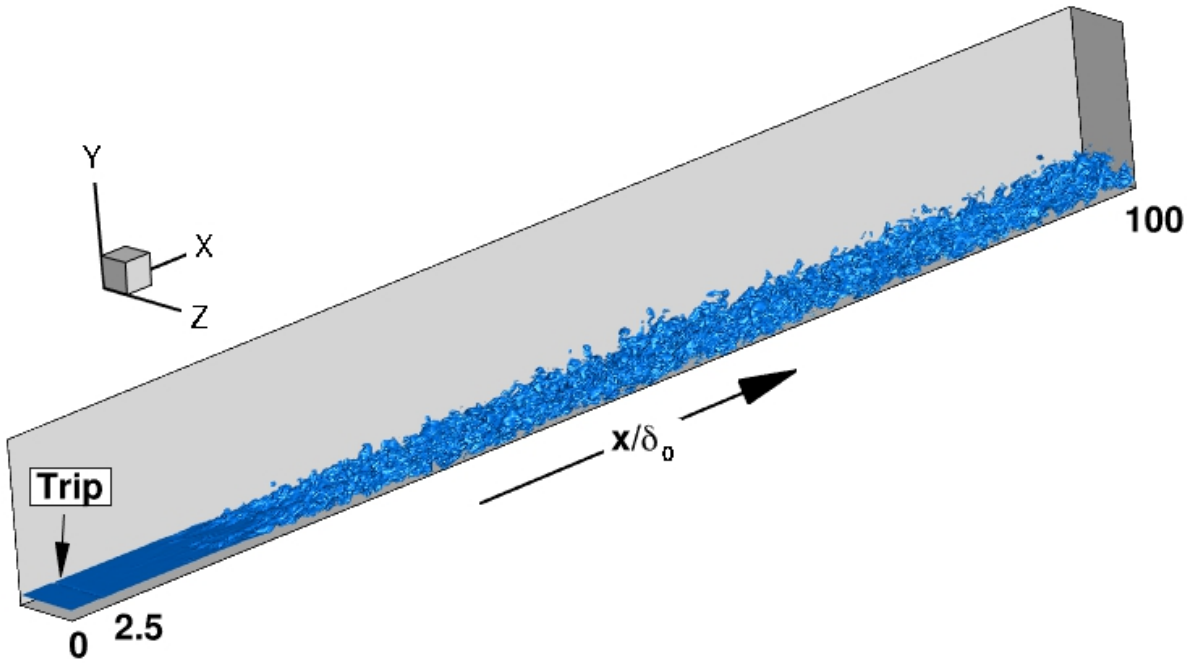

(b) Temperature isosurface, $T/T_\infty = 1.0$.

Figure 3. Overview of Mach 2.9 turbulent boundary layer flow (HOPS code, fine grid, C6/F8 scheme).

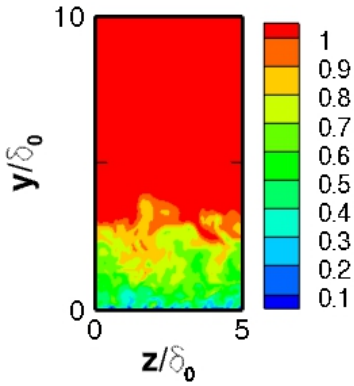

(a) End view (looking downstream): $x/\delta_0 = 100.00$ plane.

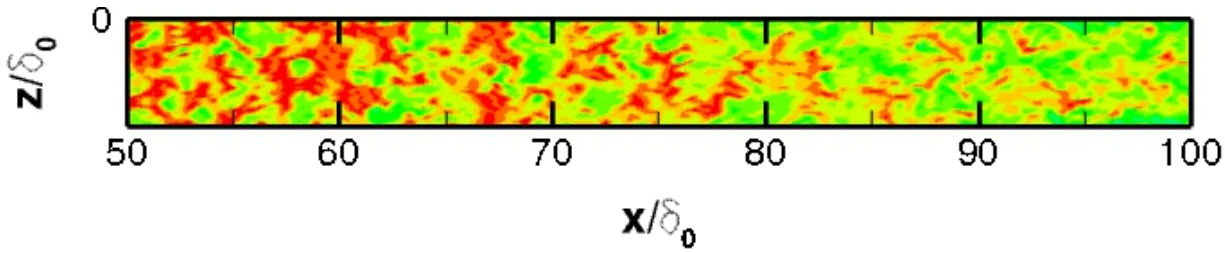

(b) Plan view (from above): $y/\delta_0 = 1.43$ ($y/\delta = 0.55$) plane.

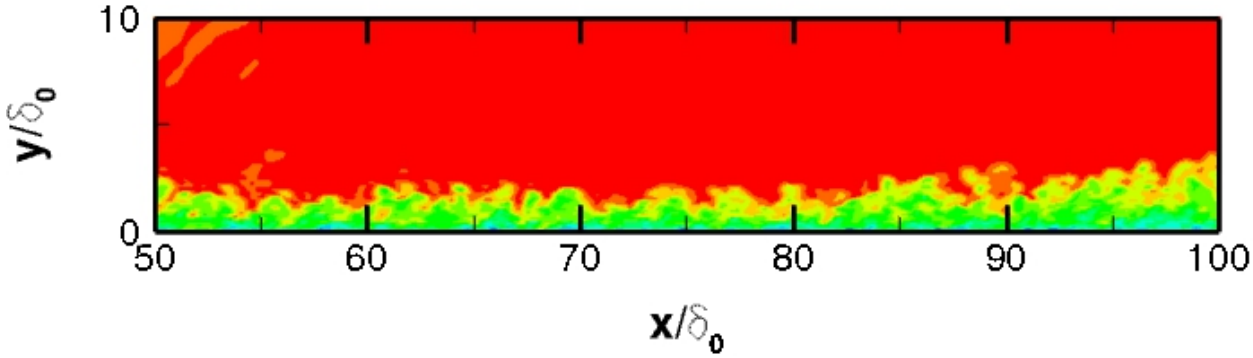

(c) Side view: $z/\delta_0 = 2.50$ plane.

Figure 4. Contour plots of the instantaneous, streamwise component of mass flux, $\rho u/(\rho_\infty u_\infty)$ (HOPS code, fine grid, C6/F8 scheme).

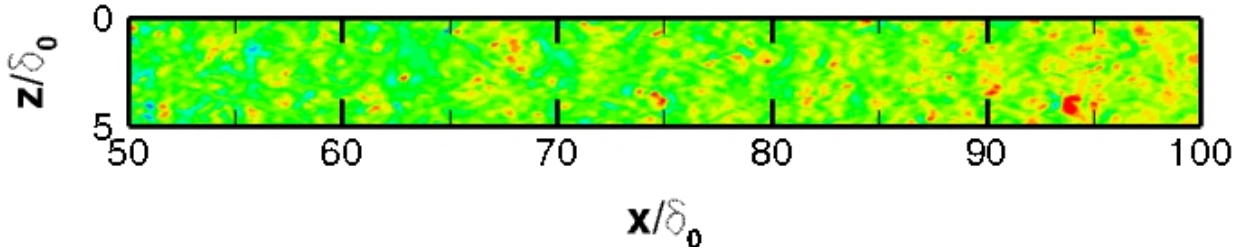

(a) Pressure, p_w.

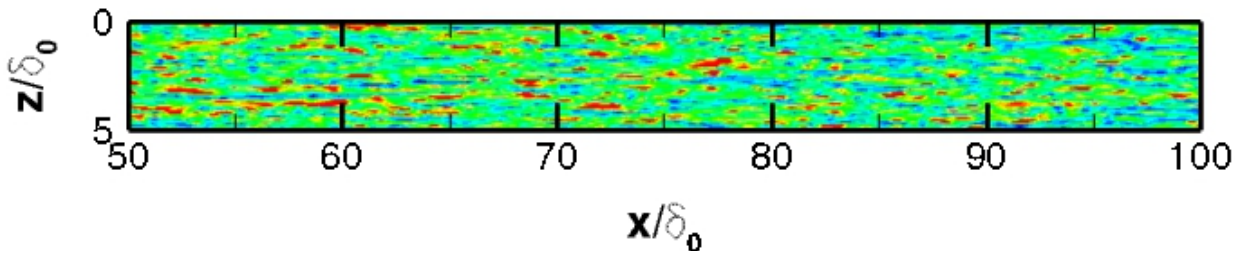

(b) Shear stress, τ_w.

Figure 5. Instantaneous contours of flow properties at the wall (plan view from above, $y = 0$, HOPS code, fine grid, C6/F8 scheme).

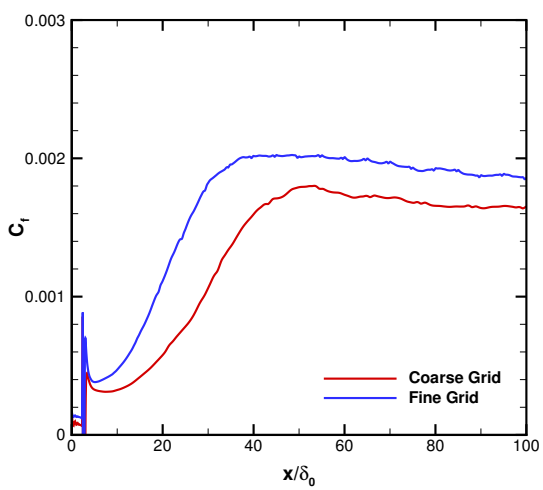

(a) Mean skin friction coefficient.

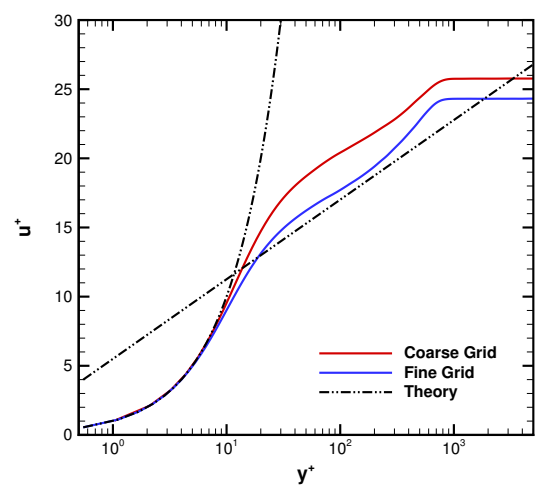

(b) Mean streamwise velocity profiles in van Driest transformed inner coordinates ($x/\delta_0 = 100$).

Figure 6. Mean flow properties of Mach 2.9 turbulent boundary layer for different grids (HOPS code, C6/F8 scheme).

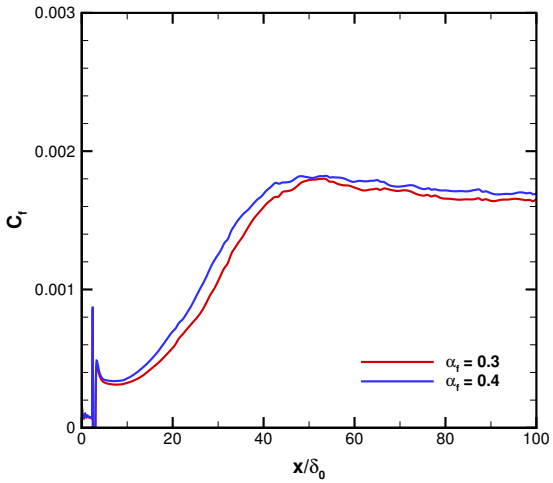

(a) Mean skin friction coefficient.

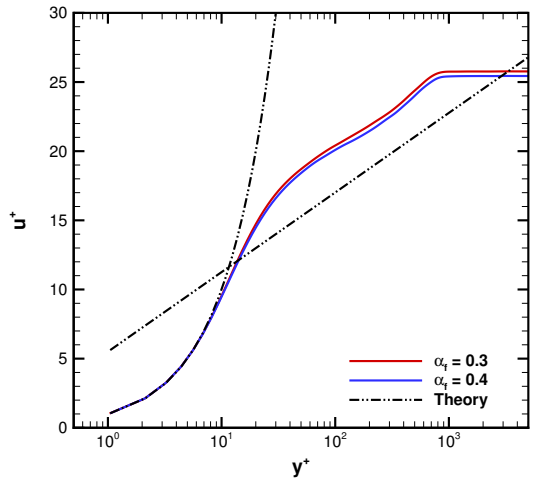

(b) Mean streamwise velocity profiles in van Driest transformed inner coordinates ($x/\delta_0 = 100$).

Figure 7. Mean flow properties of Mach 2.9 turbulent boundary layer for different filter coefficients (HOPS code, coarse grid, C6/F8 scheme).

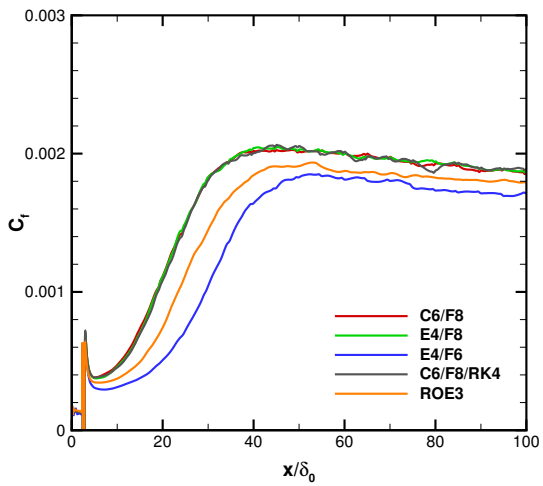

(a) Mean skin friction coefficient.

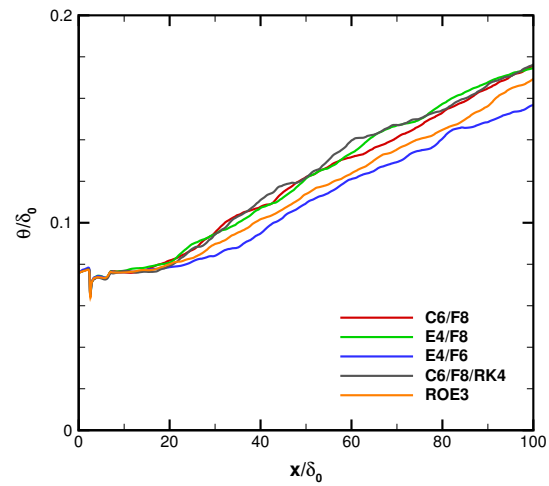

(b) Mean momentum thickness.

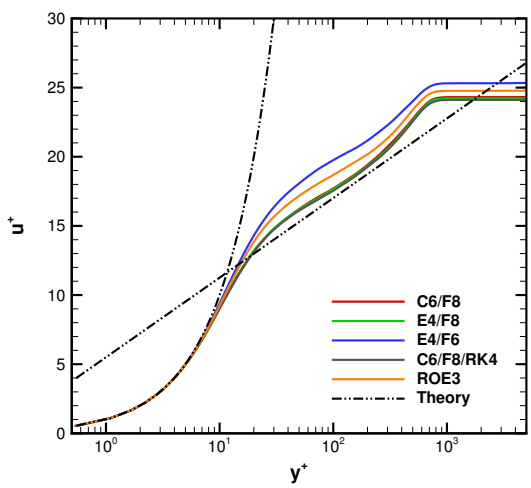

(c) Mean streamwise velocity profiles in van Driest transformed inner coordinates ($x/\delta_0 = 100$).

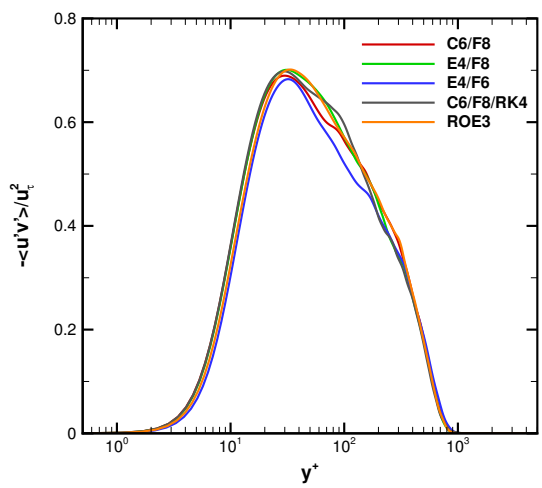

(d) Mean Reynolds stress in inner coordinates ($x/\delta_0 = 100$).

Figure 8. Mean flow properties of Mach 2.9 turbulent boundary layer for different numerical schemes (HOPS code, fine grid).

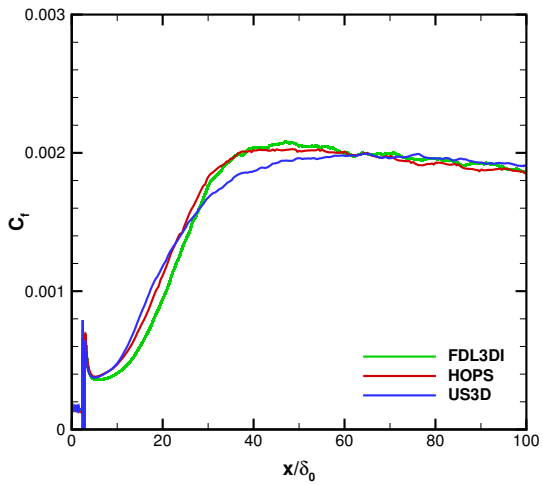

(a) Mean skin friction coefficient.

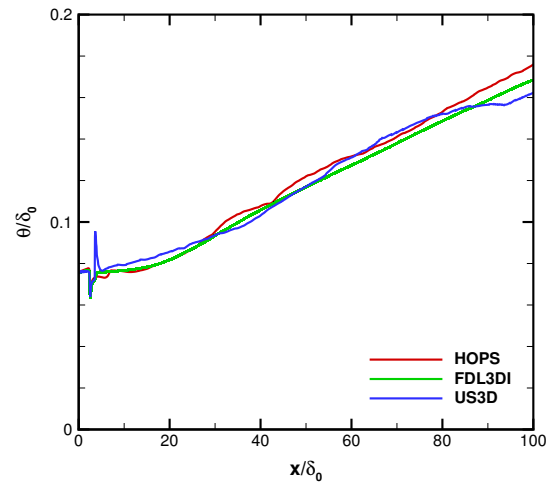

(b) Mean momentum thickness.

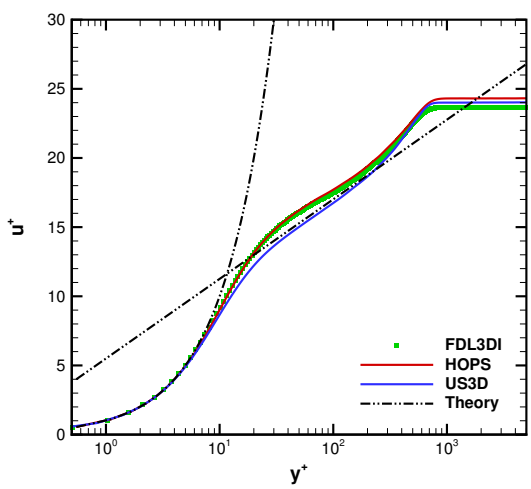

(c) Mean streamwise velocity profiles in van Driest transformed inner coordinates ($x/\delta_0 = 100$).

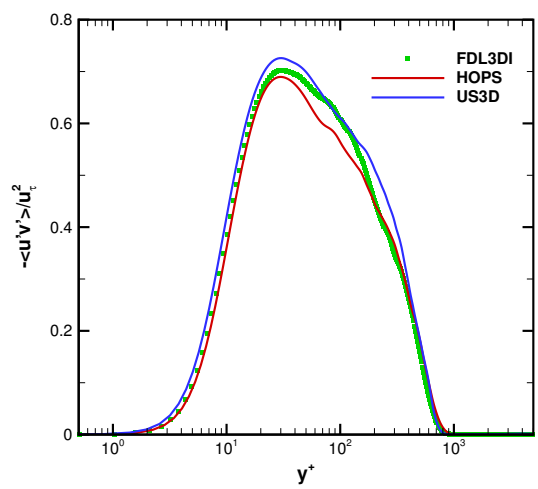

(d) Mean Reynolds stress in inner coordinates ($x/\delta_0 = 100$).

Figure 9. Mean flow properties of Mach 2.9 turbulent boundary layer for computations on fine grid with different codes.

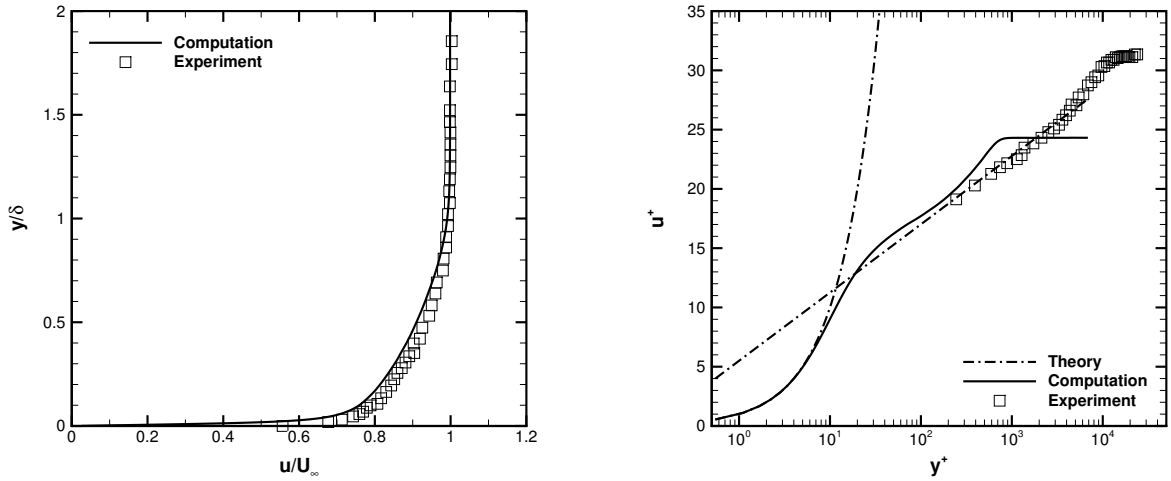

(a) Outer variables.

(b) Van Driest transformed inner variables.

Figure 10. Mean velocity profiles obtained with HOPS code ($\mathrm{Re}_\theta = 5.7 \times 10^3$) compared to experimental data of Figure 3-5 of Spina[24] ($\mathrm{Re}_\theta = 8.1 \times 10^4$).

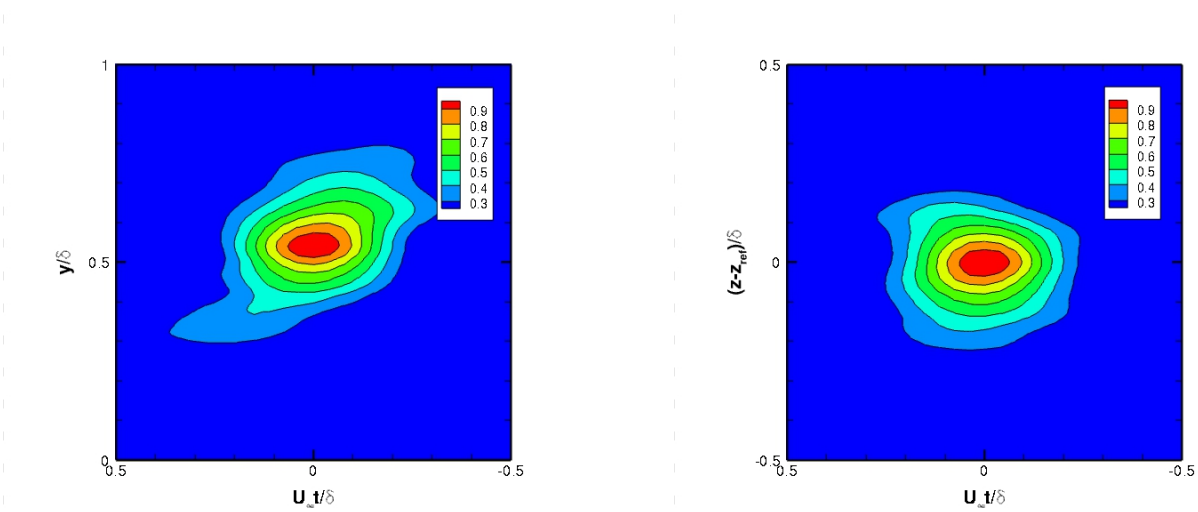

(a) Side view, $z/\delta_0 = 2.50$.

(b) Plan view, $y/\delta = 0.55$.

Figure 11. Space-time correlations of streamwise component of mass flux $(\rho u)'$.

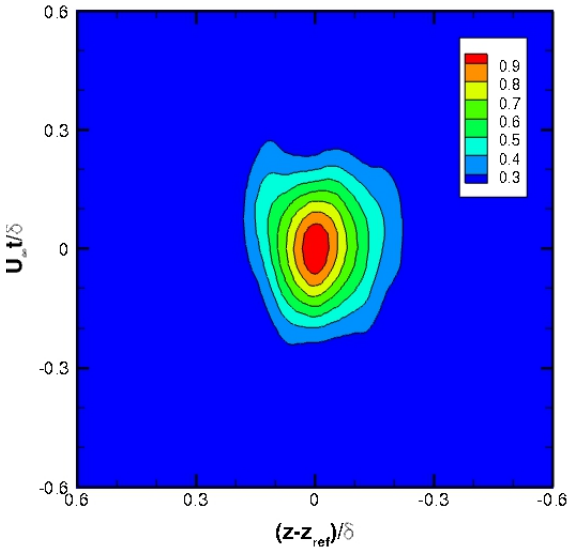

(a) Computation, $y/\delta = 0.55$, $\mathrm{Re}_\theta = 5.7 \times 10^3$.

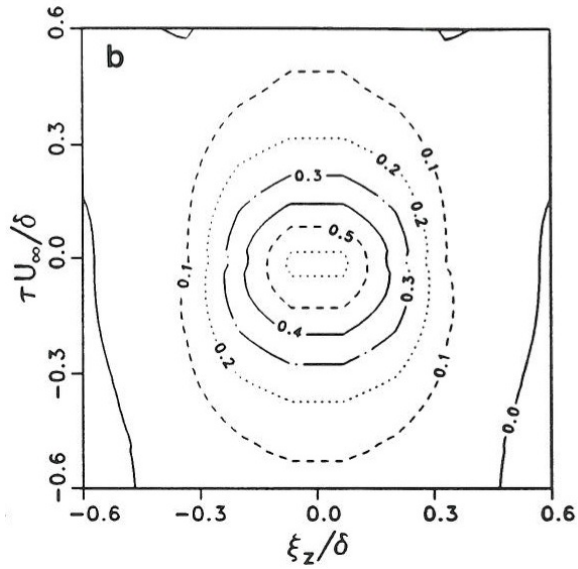

(b) Experiment, $y/\delta = 0.51$, $\mathrm{Re}_\theta = 8.1 \times 10^4$. Figure 4-29 of Spina.[24]

Figure 12. Space-time correlations of streamwise component of mass flux $(\rho u)'$ for a plane parallel to the wall.

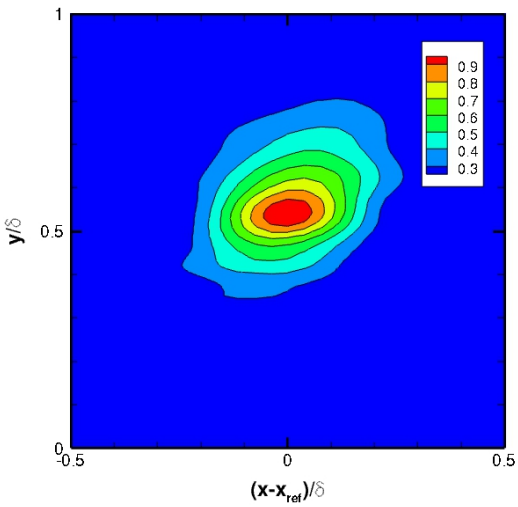

(a) Side view ($z/\delta_0 = 2.50$ plane).

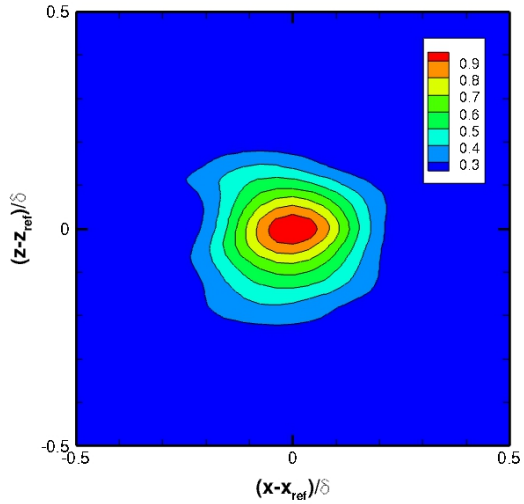

(b) Plan view ($y/\delta = 0.55$ plane).

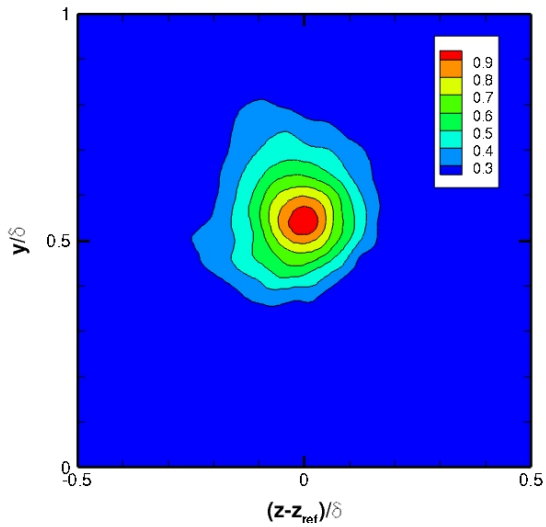

(c) End view ($x/\delta_0 = 100$ plane).

Figure 13. Two-point, spatial correlations of streamwise component of mass flux $(\rho u)'$. Reference station: $x_{\mathrm{ref}}/\delta_0 = 97.0$, $y_{\mathrm{ref}}/\delta = 0.55$, $z_{\mathrm{ref}}/\delta_0 = 2.5$.

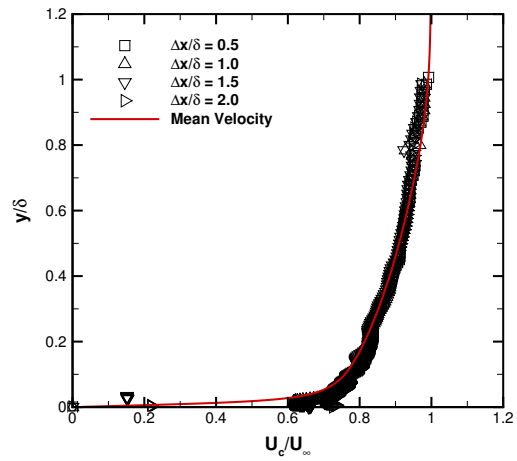

(a) Computations, $x_{\mathrm{ref}}/\delta_0 = 98.0$, $\mathrm{Re}_\theta = 5.6 \times 10^3$.

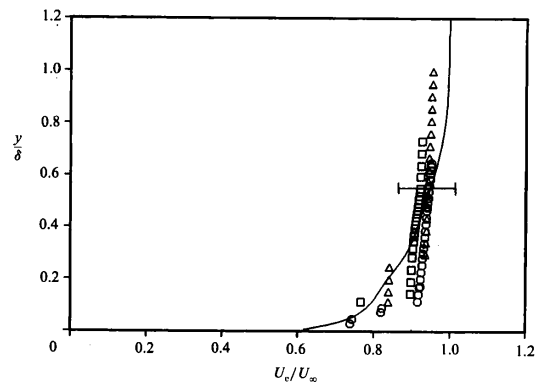

(b) Experiment, $\mathrm{Re}_\theta = 8.1 \times 10^4$. Symbols: □, $\Delta x/\delta = 0.11$; ◯, $\Delta x/\delta = 0.16$; △, $\Delta x/\delta = 0.18$; line, mean velocity. (Figure 3 of Spina et al.,[33] used under the terms of the Cambridge University Press for the reproduction of a single figure.)

Figure 14. Broad-band convection velocity, based on mass flux fluctuations $(\rho u)'$.

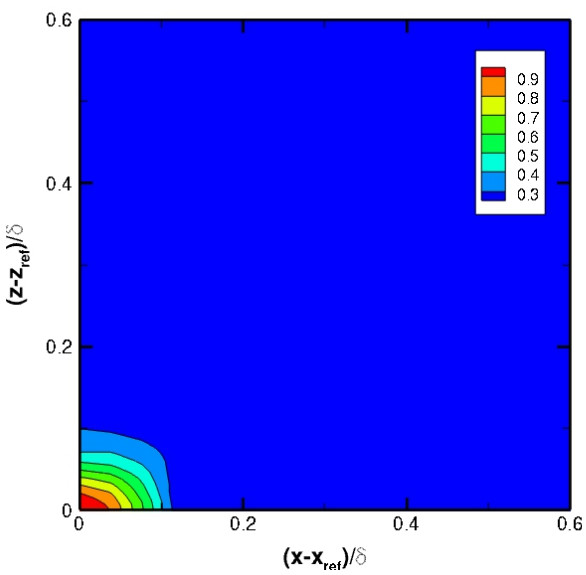

(a) Computations, $\mathrm{Re}_\theta = 5.7 \times 10^3$. Reference station: $x_{\mathrm{ref}}/\delta_0 = 97.0$, $z_{\mathrm{ref}}/\delta_0 = 2.5$.

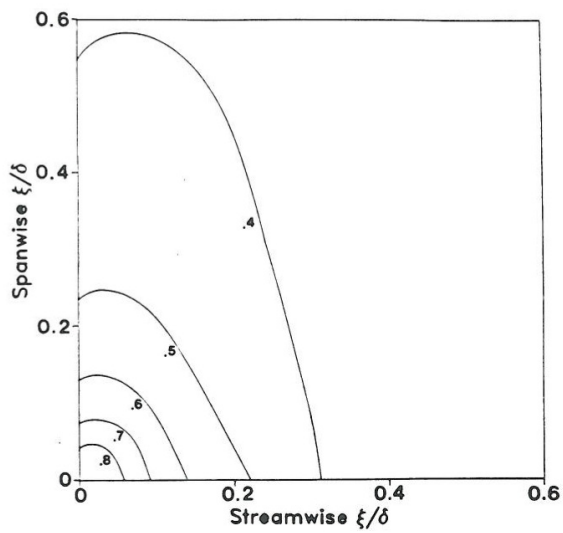

(b) Experiment, $\mathrm{Re}_\theta = 8.1 \times 10^4$. Figure 4-4 of Spina.[24]

Figure 15. Two-point spatial correlations of wall pressure fluctuations p'_w.

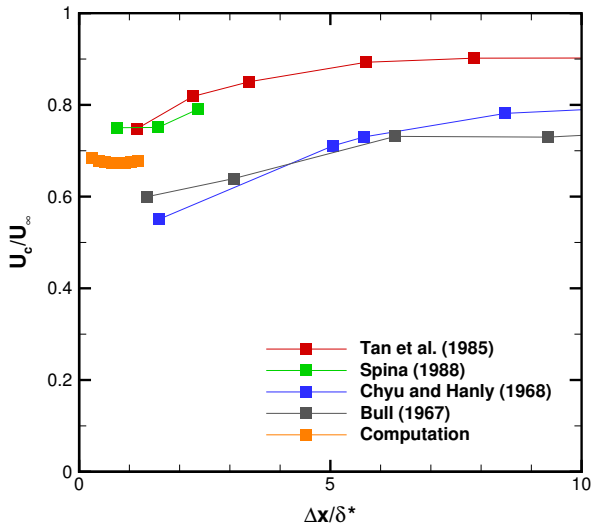

Figure 16. Broad-band convection velocity, based on wall pressure fluctuations p'_w. Reference station: $x_{\mathrm{ref}}/\delta_0 = 98.0$. Experimental data of Bull,[35] Chyu and Hanley,[36] Tan et al.,[37] and Spina.[24]